J. Indian Inst. Sci., Nov.–Dec. 2005, **85**, 391–402

Magnetic circular dichroism of the mercapto radical in noble-gas matrices

JEREMY J. HARRISON† AND BRYCE E. WILLIAMSON*
Department of Chemistry, University of Canterbury, Private Bag 4800, Christchurch, New Zealand.
e-mail: bryce.williamson@canterbury.ac.nz; Tel: ++ 64 3 364 2439; Fax: ++ 64 3 364 2110.

Abstract

Magnetic circular dichroism (MCD) and absorption spectra are reported over the temperature range ~ 1.3–25 K and at magnetic fields up to 5 T for the (0, 0) band of the $A^2\Sigma^+ \leftarrow X^2\Pi_i$ system of the mercapto radical isolated in Ar, Kr and Xe matrices. A simple model is presented in which the temperature and magnetic-field dependences of the MCD are ascribed to population differences between the levels of the $X^2\Pi_i$ term that are split by the simultaneous action of spin-orbit and crystal-field effects. This model reproduces the observed positive sign of the MCD B and C terms. However, attempts to extend it to a quantitative interpretation of the data yield poor fits and unrealistic parameters, possibly as a consequence of strong guest-host binding.

Keywords: Mercapto, magnetic circular dichroism, matrix isolation, crystal fields, spin–orbit coupling.

1. Introduction

Diatomic monohydride radicals (XH) of elements from groups 14–16 are produced by high-energy processes such as electrical discharges and vacuum-ultraviolet photolysis of suitable precursors. The second-period species, CH (methylidyne), NH (imidogen) and OH (hydroxyl), are the most common and important of these in terrestrial environments, being involved, for example, as intermediates in combustion reactions of organic materials [1]. OH is the dominant tropospheric oxidizing agent; it is involved in many atmospheric reactions and is responsible for ~20% of natural ozone loss [2]. The complete set of period-2 and -3 radicals have been observed spectroscopically in the atmospheres of stars [3–11], while CH, NH, OH [12] and SH (mercapto) [11] have also been detected in the interstellar medium.

XH spectra are well known from the gas-phase [13], but accounts of the condensed-phase spectroscopy are limited. We have previously reported magnetic circular dichroism (MCD) and absorption spectra of the second-period radicals CH [14], NH [15,16], and OH [17] isolated in inert-gas matrices at cryogenic temperatures over a range of magnetic-field strengths. The results were interpreted in the framework of a model in which spin–orbit (SO) and/or spin–spin (SS) coupling of the radicals in a randomly oriented ensemble are modified by guest–host interactions and dynamics of the guest. More recently, we extended this treatment to the third-period species, PH isolated in Ar, Kr and Xe [18], again with remarkable success. In this work, we report further extension of the treatment to SH in Ar, Kr and Xe matrices.

*Author for correspondence.
†Present address: Physical and Theoretical Chemistry Laboratory, University of Oxford, South Parks Road, Oxford, OX1 3QZ, United Kingdom.

In 1939, Lewis and White inferred the presence of gas-phase SH radicals from a $^2\Sigma^+ \leftarrow {}^2\Pi_i$ band system at ~ 324 nm in the absorption spectrum of H_2S subjected to a pulsed, radio-frequency discharge [19]. This result completed the detection of the full set of neutral second- and third-row monohydrides, apart from those of the noble-gas elements. High-resolution absorption spectra of the (0, 0) and (1, 0) bands of the $A^2\Sigma^+ \leftarrow X^2\Pi_i$ systems of SH and SD were subsequently measured by Ramsay and coworker [20, 21], who derived molecular parameters and found that the excited states undergo rapid predissociation.

The first report of the electronic spectroscopy of matrix-isolated SH and SD appeared in 1970, when Acquista and Schoen published transition wavenumbers obtained from the absorption spectra of radicals that were produced by gas-phase photolysis and trapped in solid Ar at 20.4 K [22]. More recently, emission and excitation spectra have been reported by Zoval *et al*. for SH in Ar and Kr [23] and by Khriachtev *et al*. for SH in Ne, Ar, Kr and Xe [24].

In this paper, MCD and absorption spectra are reported for SH in noble-gas matrices (SH/NG; NG = Ar, Kr, Xe) at accurately determined temperatures between ~ 1.3 and 25 K, and at magnetic fields up to 5 T.

2. Experimental

MCD (ΔA) and double-beam absorption (A) spectra were measured simultaneously using a previously described spectrometer [15, 17], equipped with a Xe-arc lamp, a 1180-groove/mm grating blazed at 300 nm, a Hamamatsu R-376 PMT and at a spectral resolution of 0.2 nm (~20 cm^{-1}). ΔA is the difference between the absorbance of left (A_+) and right (A_-) circularly polarized light by a sample in the presence of a longitudinal magnetic field of inductance B, while A is the corresponding average absorbance [25];

$$\Delta A = A_+ - A_- \tag{1}$$

$$A = (A_+ + A_-)/2 \tag{2}$$

Preliminary experiments to optimise the sample preparation conditions were conducted by using an APD Cryogenics closed-cycle He refrigerator placed between the poles of a 0.7-T Alpha Magnetics 4800 electromagnet. H_2S vapour (Aldrich, 99.5%) was mixed in a ~1 : 300 mole ratio with Ar or a ~ 1 : 100 ratio with Kr or Xe to give a total pressure of ~ 1 atm. The mixture was allowed to flow through a 12-mm (i.d.) glass tube at the rate of ~ 2-3 mmol h^{-1} while being subject to resonance radiation produced by a Tesla-coil discharge. The products were deposited for ~ 45 min onto a cryogenically cooled *c*-cut sapphire sample window held at ~20 K.

The final experiments used an Oxford Instruments SM4 cryomagnet in a matrix-injection mode that is described elsewhere [26, 27]. Temperatures above 4.2 K were obtained by operating the SM4 sample chamber as a continuous-flow cryostat, using cold He vapour as the exchange gas and monitoring the temperature with a carbon resistance thermometer. Lower temperatures were achieved by filling the sample chamber with liquid He, then pumping the vapour with a rotary vane vacuum pump while controlling the pressure with an Oxford Instruments MNT manostat. The temperature of the liquid cryogen was determined from the head-space vapour pressure [28], as measured by a MKS Baratron 1000-Torr capacitance manometer.

3. Results

Figures 1–3 show the (temperature-independent) absorption spectra and the temperature dependence of the MCD (at $B \approx 1$ T) for the (0, 0) bands of the $A^2\Sigma^+ \leftarrow X^2\Pi_i$ transitions of

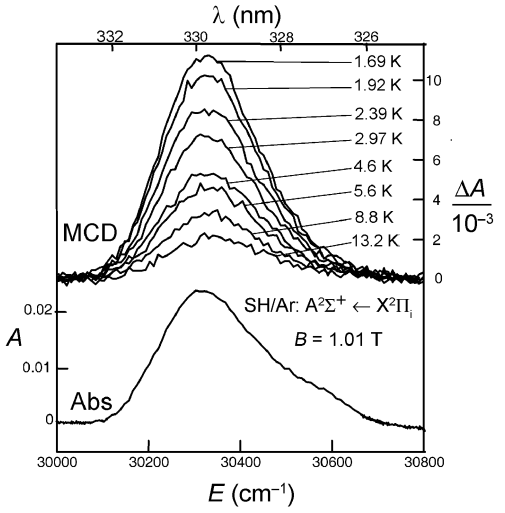

FIG. 1. Absorption spectrum (bottom) and temperature-dependent MCD spectra (at 1.01 T; top) of the (0, 0) band of the $A^2\Sigma^+ \leftarrow X^2\Pi_i$ system of SH/Ar.

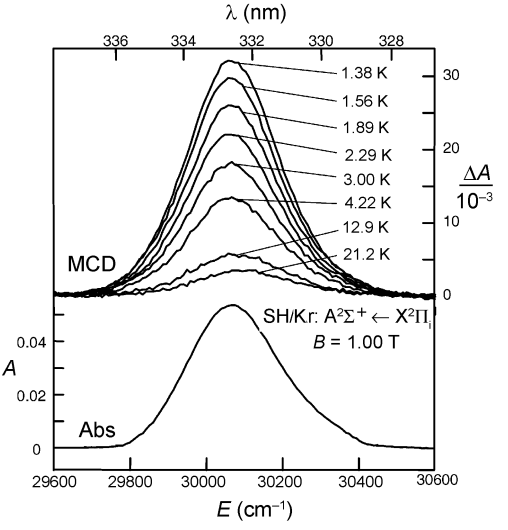

FIG. 2. Absorption spectrum (bottom) and temperature-dependent MCD spectra (at 1.00 T; top) of the (0, 0) band of the $A^2\Sigma^+ \leftarrow X^2\Pi_i$ system of SH/Kr.

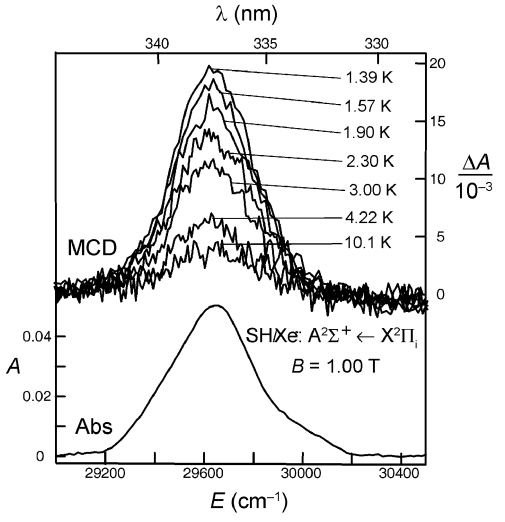

FIG. 3. Absorption spectrum (bottom) and temperature-dependent MCD spectra (at 1.01 T; top) of the (0, 0) band of the $A^2\Sigma^+ \leftarrow X^2\Pi_i$ system of SH/Xe.

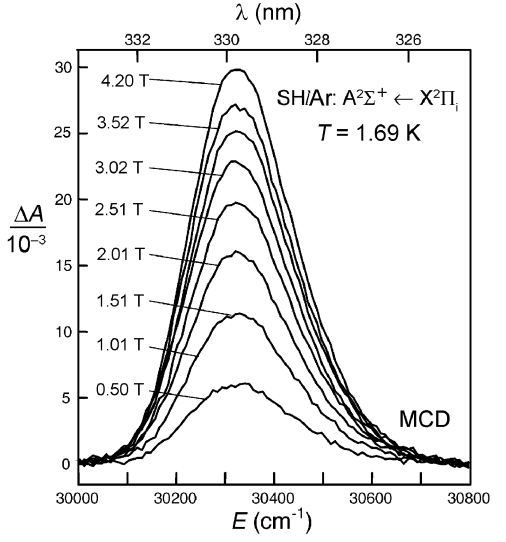

FIG. 4. Magnetic-field dependence of the MCD (at 1.69 K) of the (0, 0) band of the $A^2\Sigma^+ \leftarrow X^2\Pi_i$ system of SH/Ar.

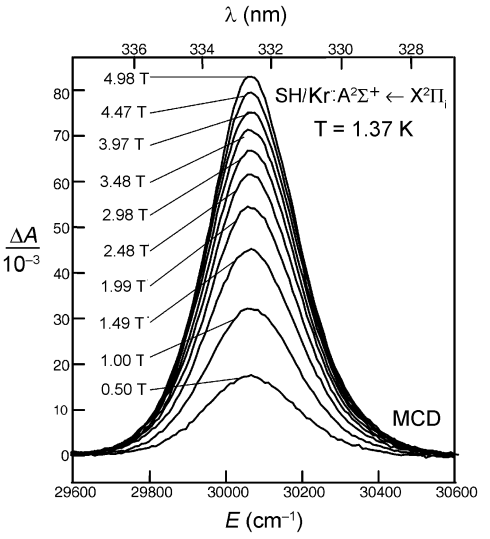

FIG. 5. Magnetic-field dependence of the MCD (at 1.37 K) of the (0, 0) band of the $A^2\Sigma^+ \leftarrow X^2\Pi_i$ system of SH/Kr.

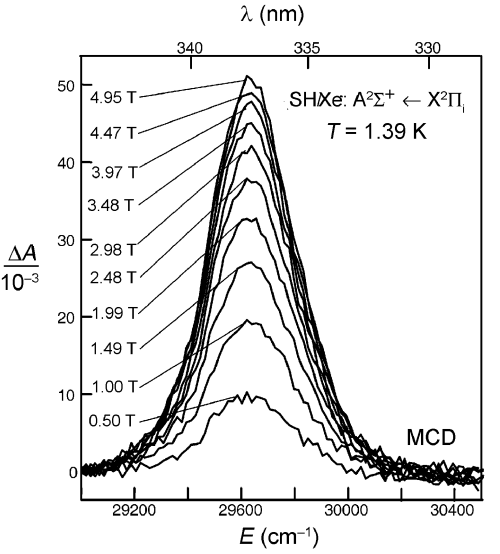

FIG. 6. Magnetic-field dependence of the MCD (at 1.39 K) of the (0, 0) band of the $A^2\Sigma^+ \leftarrow X^2\Pi_i$ system of SH/Xe.

SH/Ar, SH/Kr and SH/Xe, respectively. Each absorption spectrum exhibits a single maximum with a shoulder ~ 300 cm^{-1} to the blue. The MCD spectra are single signed and positive, showing the reciprocal temperature dependence that is characteristic of C terms and indicative of ground-state degeneracy [25]. Figures 4–6 show that the MCD increases with magnetic-field strength, but at a rate that decreases at higher fields. This type of magnetization saturation is also characteristic of C terms [25].

The spectra were quantified by using moment analysis where the *n*th absorption and MCD moments are, respectively, designated $\mathbf{A}_n$ and $\mathbf{M}_n$, as defined by eqns (3) and (4). E is the wavenumber of the radiation, $\bar{E}$ is the absorption barycenter (defined so that $\mathbf{A}_1 = 0$) and the integrals are carried over the full envelope of the band of interest.

$$\mathbf{A}_n = \int \frac{A(E - \bar{E})^n}{E} \, dE \tag{3}$$

$$\mathbf{M}_n = \int \frac{\Delta A(E - \bar{E})^n}{E} \, dE \tag{4}$$

The $\bar{E}$ values for the (0, 0) bands of each matrix are summarized in Table I, along with the absorption bandwidths, as measured by $2\sqrt{\mathbf{A}_2/\mathbf{A}_0}$. The barycenter for SH/Ar coincides with the transition wavenumber reported in absorption by Acquista and Schoen [22], while those for all three matrices are ~ 30 cm^{-1} greater than the band maxima observed in the excitation spectra [23, 24]. The bandwidths for SH/Ar and SH/Kr are also in close accord with those reported previously from excitation spectra [23].

Table I
Barycenters and bandwidths for the (0, 0) absorption bands of the $A^2\Sigma^+ \leftarrow X^2\Pi_i$ systems of SH/NG

Matrix	$\bar{E}$/cm^{-1}	$2\sqrt{A_2/A_0}$/cm^{-1}
SH/Ar	30400 ± 20	240 ± 10
SH/Kr	30110 ± 20	300 ± 20
SH/Xe	29660 ± 20	360 ± 20

Table II
Wavefunctions for the $A^2\Sigma^+$ and $X^2\Pi_i$ electronic states of SH

$\lvert^{2S+1}\lvert\Lambda\rvert_{\lvert\Omega\rvert}\ \Omega\rangle$	Normalized Slater determinants
$\lvert X^2\Pi_{1/2} \pm 1/2\rangle$	$\pm \lvert s^- s^+ p_{-1}^- \ p_{\pm1}^{\mp} \ p_{+1}^+\rangle$
$\lvert X^2\Pi_{3/2} \pm 3/2\rangle$	$\lvert s^- s^+ p_{-1}^{\pm} p_{\pm1}^{\mp} p_{-1}^{\pm}\rangle$
$\lvert A^2\Sigma^+_{1/2} \pm 1/2\rangle$	$-\lvert s^{\pm} p_{-1}^- \ p_{-1}^+ p_{+1}^- p_{+1}^+\rangle$

The intensities of the bands are measured by the dimensionless zeroth-moment parameters $\mathbf{A}_0$ and $\mathbf{M}_0$, which are effectively the areas under the absorption and MCD bands. $\mathbf{M}_0$ comprises two contributions, $\mathbf{B}_0$ and $\mathbf{C}_0$, arising from B and C terms, respectively [25];

$$\mathbf{M}_0 = \mathbf{B}_0 + \mathbf{C}_0. \tag{5}$$

$\mathbf{B}_0$ results from second-order magnetic-field-induced mixing of states and (in the absence of low-lying excited states) is temperature independent. $\mathbf{C}_0$ is due to the different populations of the Zeeman-split levels of the ground-state term and is therefore both temperature and magnetic-field dependent. $\mathbf{C}_0$ is nearly always the dominant contributor to $\mathbf{M}_0$ for paramagnetic systems; and the temperature dependence of the MCD in Figs 1–3 and the magnetization saturation behaviour in Figs 4–6 shows this to be the case for the $A^2\Sigma^+ \leftarrow X^2\Pi_i$ transitions of SH/NG.

Zeroth moments were determined numerically for the (0, 0) bands of each of the samples. Plots of the resultant $\mathbf{M}_0/\mathbf{A}_0$ ratios against $m_B B/2kT$ (m_B is the Bohr magneton and k is Boltzmann's constant) are given in Figs 7–9, where the C-term saturation behaviour is clearly evident. For SH/Ar (as for OH/Ar [17]), the data essentially conform to a single curve, independent of temperature or magnetic field. But for SH/Kr and SH/Xe, the data fall on to 'isomagnetic' curves, which change from one magnetic field to another. The fact that the curves move to higher values with increasing field indicates the presence of positive B terms (of the same sign as the C terms), which, although weak, are far from negligible.

4. Discussion

The $A^2\Sigma^+ \leftarrow X^2\Pi_i$ transitions of SH arise from the $2p \leftarrow 5s$ excitation. The bases states for the electronic states within these terms are defined in Table II, where $|\Lambda|$ represents the absolute projection of the orbital angular momentum along the internuclear (z) axis ($|\Lambda|$ is 0 for Σ states and 1 for Π states), S is the total spin quantum number, and Ω, the component of the total electronic angular momentum along z.

The twofold degeneracy of the $A^2\Sigma^+$ term can be lowered only by a magnetic field (Fig. 10), but the ground-state term can be split by a number of other mechanisms. In the gas-phase, the $X^2\Pi_i$ term separates into two electronic spin-orbit (SO) levels quantized by $|\Omega|$ (= 1/2, 3/2) and having energies given by,

$$E_{SO}(^2\Pi_{|\Omega|}) = A_\Pi(|\Omega| - 1) \tag{6}$$

where A_Π is the SO coupling constant, which has a value of –376 cm^{-1} in the gas phase [20, 29].

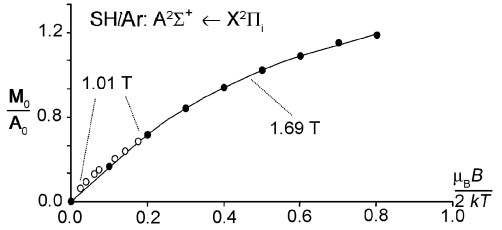

FIG. 7. The moment ratio $\mathbf{M}_0/\mathbf{A}_0$ as a function of $m_B B/kT$ for the (0, 0) band of SH/Ar $A^2\Sigma^+ \leftarrow X^2\Pi_i$. Open circles represent data obtained by varying the temperature at a constant magnetic field of 1.01 T, while closed circles were obtained by changing the magnetic field at 1.69 K. The curve is a fit to all data using the SO-CF model with unconstrained K and the parameters shown in Table III.

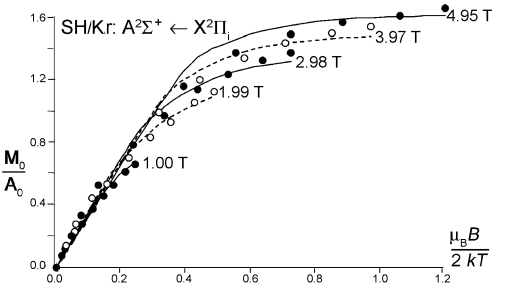

FIG. 8. The moment ratio $\mathbf{M}_0/\mathbf{A}_0$ as a function of $m_B B/2kT$ for the (0, 0) band of SH/Kr $A^2\Sigma^+ \leftarrow X^2\Pi_i$. The curves are fits to all data using the SO-CF model with unconstrained K and the parameters shown in Table III. The differences between the isomagnetic curves are due to the presence of B terms.

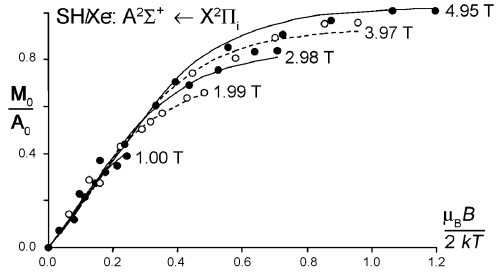

FIG. 9. The moment ratio $\mathbf{M}_0/\mathbf{A}_0$ as a function of $m_B B/2kT$ for the (0, 0) band of SH/Xe $A^2\Sigma^+ \leftarrow X^2\Pi_i$. The curves are fits to all data using the SO-CF model with unconstrained K and the parameters listed in Table III. The differences between the isomagnetic curves are due to the presence of B terms.

When SH is incorporated into condensed media, $X^2\Pi_i$ is also susceptible to first-order crystal-field (CF) effects involving the orthorhombic component of the electric field due to neighbouring host atoms [17]. This induces mixing between the SO levels, with the nonzero matrix elements being

$$\langle X^2\Pi_{3/2} \pm 3/2|H_{CF}|\ X^2\Pi_{1/2}\ \mathbf{m}\ 1/2\rangle = \mathbf{m}V_\Pi/2. \tag{7}$$

The combined SO-CF splitting of the $X^2\Pi$ manifold (Fig. 10) is

$$\Delta = (A_\Pi^2 + V_\Pi^2)^{1/2} \tag{8}$$

where the value of A_Π will be modified from the gas-phase values [14–18].

The upper and lower SO-CF levels are, respectively, designated $^2\Pi_+$ and $^2\Pi_-$. The corresponding eigenstates are

$$|^2\Pi_+ \pm 1/2\rangle = a\ |^2\Pi_{1/2}\ \mathbf{m}\ 1/2\rangle \pm b\ |^2\Pi_{3/2} \pm 3/2\rangle \tag{9}$$

$$|^2\Pi_- \pm 1/2\rangle = a\ |^2\Pi_{3/2}\ \mathbf{m}\ 3/2\rangle\ \mathbf{m}\ b\ |^2\Pi_{1/2}\ \mathbf{m}\ 1/2\rangle \tag{10}$$

where $\pm 1/2$ in the left-hands kets indicates the values of Σ, the projection of the electronic spin along z. The mixing coefficients are

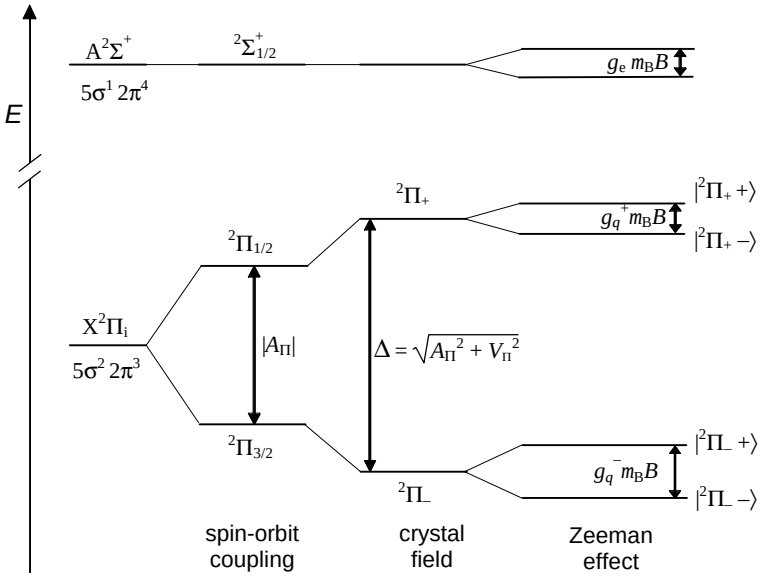

FIG. 10. Energy-level diagram for the $X^2\Pi_i$ and $A^2\Sigma^+$ terms of SH/NG showing the effects of spin-orbit, crystal-field and Zeeman interactions.

$$a = ((1 + k)/2)^{1/2} \tag{11}$$

$$b = ((1 - k)/2)^{1/2} \tag{12}$$

k is defined by

$$k = -A_\Pi/\Delta \tag{13}$$

and (with $A_\Pi < 0$) takes values $0 \le k \le 1$, depending on the relative strengths of the SO and CF effects.

In an external magnetic field, the remaining degeneracies of the $X^2\Pi_i$ term are lifted by first-order Zeeman splittings that depend on the angle, q, that the internuclear (z) axis makes with the magnetic field (Z) direction. The appropriate eigenfunctions and their Zeeman energies are

$$|^2\Pi_s\pm\rangle = a_s|^2\Pi_s\pm\tfrac{1}{2}\rangle \pm b_s|^2\Pi_s\mp\tfrac{1}{2}\rangle \tag{14}$$

$$E_B^q(^2\Pi_s\pm) = \pm\, g_q^s\, m_B B/2. \tag{15}$$

In eqns (14) and (15), s corresponds to the ± labels for the upper and lower SO-CF levels (as shown in Fig. 10) and the g values are

$$g_q^\pm = ((g_\parallel^\pm \cos q)^2 + (g_\perp \sin q)^2)^{1/2} \tag{16}$$

$$g_\parallel^\pm = 2\langle{}^2\Pi_\pm + \tfrac{1}{2}|L_z + g_e S_z|{}^2\Pi_\pm + \tfrac{1}{2}\rangle = g_e\mp 2k \tag{17}$$

$$g_\perp = 2\langle{}^2\Pi_\pm + \tfrac{1}{2}|L_x + g_e S_x|{}^2\Pi_\pm - \tfrac{1}{2}\rangle = g_e(1 - k^2)^{1/2}. \tag{18}$$

The mixing coefficients in eqn (14) satisfy the relationships

$$|a_{\pm}|^2 = (g_{\perp}\sin q)^2/(2g_q^{\pm}(g_q^{\pm} - g_{\parallel}^{\pm}\cos q)) \tag{19}$$

$$|a_{\pm}|^2 + |b_{\pm}|^2 = 1 \tag{20}$$

$$|a_{\pm}|^2 - |b_{\pm}|^2 = g_{\parallel}^{\pm}\cos q/g_q^{\pm}. \tag{21}$$

According to eqn (17), k can be regarded as an orbital reduction factor for the lower ($^2\Pi_-$) SO-CF level. In the absence of a CF, $k = 1$, both $g_{\perp}$ and (in the approximation $g_e \approx 2.00$) $g_{\parallel}^{\pm}$ vanish, and the Zeeman splitting of the lower ($^2\Pi_- = {}^2\Pi_{3/2}$) level is a simple cosine function of q. In the strong-CF limit ($k \to 0$), the orbital angular momentum is totally quenched, all g values take the spin-only value (g_e) and the Zeeman splittings of the two SO-CF levels are equal and isotropic.

In the following, expressions are presented for the zeroth moments $\mathbf{A}_0$, $\mathbf{B}_0$ and $\mathbf{C}_0$ in terms of transition moments, temperature and magnetic-field strength. The treatment parallels one presented elsewhere for OH/Ar [17], but is generalized to include transitions originating from the upper ($^2\Pi_+$) SO-CF level of the ground-state term [30]. The starting point is the definition of $\mathbf{A}_+^q$ and $\mathbf{A}_-^q$, respectively, the absorbance moments of left and right circularly polarized transitions for a molecule at angle q with respect to Z. Using the principle of spectroscopic stability [25] in choosing the excited-state functions in the SO basis, these are given by

$$\mathbf{A}_{\pm}^q = g\sum_s\sum_{\Omega}(P_s^q(+)|\langle {}^2\Sigma^+\Omega|M_{\pm 1}|{}^2\Pi_s+\rangle|^2 + P_s^q(-)|\langle {}^2\Sigma^+\Omega|M_{\pm 1}|{}^2\Pi_s-\rangle|^2). \tag{22}$$

The parameter g contains a number of constant factors, including the concentration and path length of the sample. $M_{\pm 1} = \mathbf{m}(2)^{-1/2}(M_X \pm iM_Y)$ are circularly polarised components of the electric-dipole operator in a laboratory-fixed reference frame and $P_\sigma^q(\pm)$ are the fractional Boltzmann populations of states $|{}^2\Pi_s \pm\rangle$;

$$P_\sigma^q(\pm) = \frac{1}{Q^q}\exp\left(\frac{-s\Delta\,\mathbf{m}\,g_q^-m_BB}{2kT}\right) \tag{23}$$

where Q^q is the electronic partition function;

$$Q^q = 2\cosh\left(\frac{g_q^-m_BB}{2kT}\right)\exp(\Delta/2kT) + 2\cosh\left(\frac{g_q^+m_BB}{2kT}\right)\exp(-\Delta/2kT). \tag{24}$$

Transforming to the molecular reference frame and summing over all contributions, the corresponding zeroth moments are

$$\mathbf{A}_0^q = (\mathbf{A}_+^q + \mathbf{A}_-^q)/2 = g\,(1 + \cos^2 q)\,|\mathrm{M}|^2/8 \tag{25}$$

$$\mathbf{C}_0^q = \mathbf{A}_+^q - \mathbf{A}_-^q$$

$$= \frac{gk\cos^2 q\,|\mathrm{M}|^2}{Q^q}\left[\frac{g_{\parallel}^-}{g_q^-}\sinh\left(\frac{g_q^-m_BB}{2kT}\right)\exp(\Delta/2kT) - \frac{g_{\parallel}^+}{g_q^+}\sinh\left(\frac{g_q^+m_BB}{2kT}\right)\exp(-\Delta/2kT)\right] \tag{26}$$

where $\mathrm{M} = \langle p\|m\|s\rangle$ is the one-electron, reduced, electric-dipole transition moment for $2p \leftarrow 5s$ in the molecular reference frame. Determination of the corresponding expression

for $\mathbf{B}_0$ requires consideration of the magnetic-field-induced mixing of the Zeeman states $|^2\Pi_s \pm\rangle$, which gives the result,

$$\mathbf{B}_0^q = \frac{g\,(g_\perp \cos q)^2 m_B B |M|^2}{2\Delta Q^q}\left[\cosh\left(\frac{g_q^- m_B B}{2kT}\right)\exp(\Delta/2kT) - \cosh\left(\frac{g_q^+ m_B B}{2kT}\right)\exp(-\Delta/2kT)\right]. \quad (27)$$

The moments for a randomly oriented ensemble of radicals are obtained by averaging over q. Doing this, and then taking the appropriate ratios, gives

$$\mathbf{C}_0/\mathbf{A}_0 = 3k\left[\exp(\Delta/2kT)\int_0^1 \frac{1}{Q^q}\frac{g_\parallel^- \cos^2 q}{g_q^-}\sinh\left(\frac{g_q^- m_B B}{2kT}\right)\mathrm{d}\cos q - \right.$$

$$\left. \exp(-\Delta/2kT)\int_0^1 \frac{1}{Q^q}\frac{g_\parallel^+ \cos^2 q}{g_q^+}\sinh\left(\frac{g_q^+ m_B B}{2kT}\right)\mathrm{d}\cos q\right]; \quad (28)$$

$$\mathbf{B}_0/\mathbf{A}_0 = \frac{3m_B B}{\Delta}\left[\exp(\Delta/2kT)\int_0^1 \frac{1}{Q^q}(g_\perp \cos q)^2 \cosh\left(\frac{g_q^- m_B B}{2kT}\right)\mathrm{d}\cos q - \right.$$

$$\left. \exp(-\Delta/2kT)\int_0^1 \frac{1}{Q^q}(g_\perp \cos q)^2 \cosh\left(\frac{g_q^+ m_B B}{2kT}\right)\mathrm{d}\cos q\right]. \quad (29)$$

The first and second terms within the square brackets of eqns (28) and (29) pertain, respectively, to transitions originating from the $^2\Pi_-$ and $^2\Pi_+$ levels. Since the integrands are inherently positive and the contributions from the lower SO-CF level are always the larger (due to a greater Boltzmann population), these expressions indicate that both the B and C terms will be positive, in agreement with the experimental observations.

Equations (28) and (29) are functions of only two independent parameters. Choosing these to be A_Π and V_Π, least-squares fits to the $\mathbf{M}_0/\mathbf{A}_0$ data of Figures 7–9 were attempted using steepest-descent methods with the integrals evaluated by Simpson's rule. In marked contrast to the previous, successful application of this type of model to XH/NG systems [14–18], these efforts failed to yield parameters that could be regarded as realistic. With V_Π fixed at zero, the C-term, saturation behavior could be modeled, but without providing useful information about the value of A_Π. Since the $^2\Pi_{3/2}$ and $^2\Pi_{1/2}$ states are not mixed in the absence of CF interactions, the calculated temperature and magnetic-field dependences of $\mathbf{M}_0/\mathbf{A}_0$ are insensitive to A_Π until the $^2\Pi_+$ level gains an appreciable population; that is for $A_\Pi \lesssim 10\ \mathrm{cm}^{-1}$ at the temperatures used in these experiments. Additional and more significant problems emerged when attempting to account for the different isomagnetic curves in

the data for SH/Kr and SH/Xe (Figs 8 and 9). These differences arise from the positive B term contribution, which requires $g_\perp$, and hence V_Π, to be non-zero; but increasing V_Π reduces k, which, in turn, quenches the C-term. Moreover, since Δ increases with V_Π, the magnitude of the B terms increases rather slowly as V_Π increases. The counterintuitive consequence of this is that the optimum values of A_Π and V_Π for SH/Ar and SH/Xe (listed under "*K* constrained" in Table III) have much smaller magnitudes than would be expected on the basis of the SO coupling constant of gas-phase SH (–376.9 cm^{-1}) or the CF parameters (typically 50–100 cm^{-1}) found for Π terms of CH/Ar [14], NH/NG [15, 16] and PH/NG [18]. Furthermore, even with the optimized parameters, the fits for SH/Ar and SH/Xe were poor, while that for SH/Kr failed to converge.

In an attempt to improve this situation, an *ad hoc* scaling parameter, *K*, was introduced (eqn (30)), which permitted convergent and more accurate fits to be achieved. These are superimposed on the $\mathbf{M}_0/\mathbf{A}_0$ data in Figs 7–9 and the corresponding parameters are listed under "*K* unconstrained" in Table III.

$$\mathbf{M}_0/\mathbf{A}_0 = K(\mathbf{C}_0 + \mathbf{B}_0)/\mathbf{A}_0 \tag{30}$$

Putting aside concerns about the magnitudes of A_Π and V_Π, we revisited earlier results for OH/Ar [17, 31] in the context of the current work. In that earlier treatment, it was assumed (on the basis of $A_\Pi = -139$ cm^{-1} for gas-phase OH) that Δ would be large enough for transitions from the $^2\Pi_+$ level to be neglected at the low temperatures ($\lesssim 7$ K) that were used. Under these circumstances, eqns (28) and (29) reduce to simpler forms given in eqns (31) and (32) [17].

$$\mathbf{C}_0/\mathbf{A}_0 = 3k\int_0^1 \frac{g_{\|}^{-}\cos^2 q}{g_q^{-}} \tanh\left(\frac{g_q^{-} m_B B}{2kT}\right) \mathrm{d}\cos q \tag{31}$$

$$\mathbf{B}_0/\mathbf{A}_0 = g_\perp^2 m_B B/2\Delta. \tag{32}$$

Also in the assumption of large Δ, it was presumed that B terms would be small in comparison with the experimental uncertainty. The data were consequently fitted to yield $A_\Pi = -125 \pm 10$ cm^{-1} and $V_\Pi = 97 \pm 10$ cm^{-1} [17], in reasonable accord with the gas-phase SO

Table III
Best-fit SO-CF parameters obtained for SH/NG with *K* either constrained to unity or unconstrained

Matrix	*K* constrained			*K* unconstrained		
	A_Π/cm^{-1}	V_Π/cm^{-1}	*K*	A_Π/cm^{-1}	V_Π/cm^{-1}	*K*
SH/Ar	–3.4 ± 0.8	4.1 ± 0.5	1.00	–4.6 ± 1.0	8.8 ± 2.6	1.44 ± 0.22
SH/Kr[a]	–	–	1.00	–4.3 ± 0.9	6.2 ± 1.6	1.44 ± 0.16
SH/Xe	–4.1 ± 1.2	7.4 ± 1.1	1.00	–3.0 ± 0.5	3.9 ± 0.8	0.76 ± 0.06
OH/Ar[b]	–9.1 ± 7.0	8.4 ± 5.1	1.00	–6.2 ± 4.0	4.6 ± 4.5	0.88 ± 0.18

[a]Attempts to fit the SH/Kr data with the constraint $K = 1.00$ failed to converge.
[b]Parameters obtained by fitting the OH/Ar data from references [17] and [31].

coupling coefficient (–139 cm^{-1}). Having developed the expressions and software to permit explicit consideration of transitions from both SO-CF levels, we have retrospectively applied the new analysis to the old data. The best fits so obtained correspond to A_Π and V_Π values with much lower magnitudes (bottom row of Table III), which are more consistent with those obtained for SH/NG.

5. Conclusion

This work reports the MCD and absorption data for the (0, 0) band of the $A^2\Sigma^+ \leftarrow X^2\Pi_i$ system of the SH radical isolated in Ar, Kr and Xe matrices. The absorption spectra are consistent with previously reported excitation results [23, 24], while observed temperature and magnetic-field dependences of the MCD are in qualitative agreement with those expected for a linear radical with a $^2\Pi_i$ ground-state term.

A simple spin-orbit–crystal-field model, originally developed to interpret the absorption and MCD spectra of OH/Ar [17, 31], is generalized to allow for transitions arising from both the upper and lower SO-CF levels of the ground state. In agreement with experiment, the model predicts that the MCD of SH/NG is composed of positive B and C terms. However, reasonable quantitative agreement with the experimental data is possible only with the arbitrary inclusion of a scaling factor. The additional fact that spin-orbit and crystal-field parameter values so obtained are inconsistent with the gas-phase information and the results obtained for other XH radicals in noble-gas matrices indicate that the SO-CF model is inappropriate for SH/NG and probably also for OH/NG.

The reasons for the failure of the SO-CF model are not immediately clear, but it seems eminently possible that consideration must be taken of specific guest–host interactions of the type described by Zoval *et al*. in their account of laser-induced fluorescence and excitation spectra of matrix-isolated SH (and OH) in Ar and Kr matrices [23]. The experimental data presented here should provide a comprehensive basis by which to test any forthcoming and more sophisticated models.

References

1. A. G. Gaydon, *Spectroscopy and combustion theory*, Chapman and Hall (1948).
2. M. J. McEwan, and L. F. Phillips, *Chemistry of the atmosphere*, Edward Arnold (1975).
3. M. Singh, and J. P. Chaturvedi, Studies of some diatomic-molecules in the F-type and early G-type dwarf stars, *Astrophys. Space Sci*., **136**, 231–246 (1987).
4. N. Grevesse, D. L. Lambert, A. J. Sauval, E. F. Van Dishoeck, C. B. Farmer, and R. H. Norton, Identification of solar vibration-rotation lines of NH and the solar nitrogen abundance, *Astron. Astrophys*., **231**, 225–230 (1990).
5. F. Melen, A. J. Sauval, N. Grevesse, C. B. Farmer, C. Servais, L. Delbouille, and C. Roland, A new analysis of the OH radical spectrum from solar infrared observations, *J. Mol. Spectrosc*., **174**, 490–509 (1995).
6. Z. Ninkov, G. A. H. Walker, and S. Yang, The primary orbit and the absorption-lines of HDE-226868 (Cygnus X-1), *Astrophys. J*., **321**, 425–437 (1987).
7. E. M. De Gouveia, and P. D. Singh, The 3410 angstrom band of the hydrophosphorus (PH) molecule in the solar photospheric spectrum, *Solar Phys*., **90**, 259–268 (1984).

8. K. Sinha, B. M. Tripathi, R. M. Atalla, and P. D. Singh, On the possibility of faint molecular lines of phosphorus oxide (PO), phosphorus hydride (PH), magnesium hydride ion (MgH^+), and cyanogen radical in the solar spectrum, *Solar Phys*., **115**, 221–227 (1988).
9. D. N. Davis, SiH in the sun and late-type stars, *Publ. Astron. Soc. Pacific*, **52**, 280 (1940).
10. N. Grevesse, and A. J. Sauval, Oscillator strengths for SiH and SiH^+ deduced from the solar spectrum, *J. Quant. Spectrosc. Radiat. Transfer*, **11**, 65–67 (1971).
11. S. V. Berdyugina, and W. C. Livingston, Detection of the mercapto radical SH in the solar atmosphere, *Astron. Astrophys*., **387**, L6–L9 (2002).
12. D. Smith, The ion chemistry of interstellar clouds, *Chem. Rev*., **92**, 1473–1485 (1992).
13. K. P. Huber, and G. Herzberg, *Molecular spectra and molecular structure IV. Constants of diatomic molecules*, Van Nostrand Reinhold (1979).
14. V. S. Langford, and B. E. Williamson, Magnetic circular dichroism of the CH radical in an argon matrix, *J. Phys. Chem. A*, **102**, 138–145 (1998).
15. V. S. Langford, and B. E. Williamson, Magnetic circular dichroism and absorption spectra of the NH radical in an argon matrix, *J. Phys. Chem. A*, **102**, 2415–2423 (1998).
16. J. J. Harrison, B. E. Williamson, and J. L. Rose, Magneto-optical investigations of imidogen in inert-gas matrices, *J. Phys. Chem. A*, **108**, 2633–2637 (2004).
17. V. S. Langford, and B. E. Williamson, Magnetic circular dichroism of the hydroxyl radical in an argon matrix, *J. Phys. Chem. A*, **101**, 3119–3124 (1997).
18. J. J. Harrison, and B. E. Williamson, Magnetic circular dichroism and absorption spectra of phosphinidene in noble gas-matrices, *J. Phys. Chem. A*, **109**, 1343–1347 (2005).
19. M. N. Lewis, and J. U. White, The band spectrum of HS, *Phys. Rev*., **55**, 894–898 (1939).
20. D. A. Ramsay, Absorption spectra of SH and SD produced by flash photolysis of H_2S and D_2S, *J. Chem. Phys*., **20**, 1920–1927 (1952).
21. J. W. C. Johns, and D. A. Ramsay, The absorption spectrum and dissociation energy of SH, *Can. J. Phys*., **39**, 210–217 (1961).
22. N. Acquista, and L. J. Schoen, Matrix isolation spectrum of the SH radical, *J. Chem. Phys*., **53**, 1290–1291 (1970).
23. J. Zoval, D. Imre, and V. A. Apkarian, Spectroscopy of SH(A-X) transition in Ar and Kr matrices: The caging of predissociation, *J. Chem. Phys*., **98**, 1–7 (1993).
24. L. Khriachtev, M. Pettersson, E. Isoniemi, and M. Räsänen, 193 nm Photolysis products in rare-gas matrices: luminescence spectroscopy of the products, *J. Chem. Phys*., **108**, 5747–5754 (1998).
25. S. B. Piepho, and P. N. Schatz, *Group theory in spectroscopy with applications to magnetic circular dichroism*, Wiley (1983).
26. C. L. Dunford, and B. E. Williamson, Weak temperature dependence in the magnetic circular dichroism of matrix-isolated copper phthalocyanines, *J. Phys. Chem. A*, **101**, 2050–2054 (1997).
27. C. L. Dunford, *Magnetooptical and hole-burning studies of matrix-isolated metallophthalocyanines*, University of Canterbury (1997).
28. M. Durieux, and R. L. Rusby, Helium vapour pressure equations on the EPT-76, *Metrologia*, **19**, 67–72 (1983).
29. L. Veseth, Corrections to the spin-orbit splitting in $^2\Pi$ states of diatomic molecules, *J. Molec. Spectrosc*., **38**, 228–242 (1971).
30. J. J. Harrison, *Matrix-isolation magneto-optical spectroscopy of diatomic radical monohydrides*, University of Canterbury (2003).
31. V. S. Langford, *Magnetooptical spectroscopy of matrix-isolated free radicals*, University of Canterbury, (1997).